Regulated Electron-Tunneling of Photoinduced Primary Charge-Separated State in the Photosystem II Reaction Center

Masashi Hasegawa[†], *Hiroki Nagashima*[‡], *Reina Minobe*[†], *Takashi Tachikawa*[†], *Hiroyuki Mino*[‡,]*, *and Yasuhiro Kobori*[†,]*

[†]Laser Molecular Photoscience Laboratory, Molecular Photoscience Research Center, Kobe University, 1-1 Rokkodaicho Nada-ku Kobe, 657-8501 Japan.

[‡]Division of Materials Science (Physics), Graduate School of Science, Nagoya University, Furocho, Chikusa, Nagoya 464-8602, Japan.

AUTHOR INFORMATION

Corresponding Authors

*E-mail: ykobori@kitty.kobe-u.ac.jp

*E-mail: mino@bio.phys.nagoya-u.ac.jp

ABSTRACT: In initial events of the photosynthesis by higher plants, the photosystem II (PSII) generates photoinduced primary charge–separated (CS) state composed of reduced pheophytin ($Pheo_{D1}^{-\bullet}$) and oxidized special pair ($P^{+\bullet}$) in chlorophylls a (Chla) P_{D1}/P_{D2} in the D1/D2 heterodimer, ultimately leading to the water oxidation at the oxygen–evolving Mn_4CaO_5 cluster by $P^{+\bullet}$. To understand molecular mechanism of the efficient generation of the initial oxidative state, we have characterized cofactor geometries and electronic coupling of the photoinduced primary CS state in quinone pre–reduced membrane of PSII from spinach using the time-resolved EPR method. It has been revealed that that the electronic coupling between the charges is significantly weak in the CS state separated by 1.5 nm, showing an importance of regulated cofactor-cofactor electronic interaction between a vinyl substituent in $Pheo_{D1}$ and an accessory chlorophyll to inhibit the energy-wasting charge-recombination after the primary electron-transfer processes.

TOC GRAPHICS

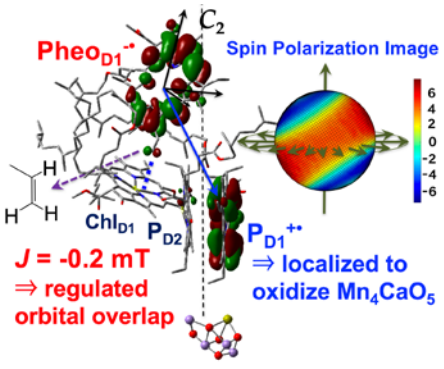

KEYWORDS plant photosynthesis • electronic coupling • cofactor geometry • pheophytin • vinyl substituent • time-resolved EPR

In the primary event of the photosynthesis by green plants and cyanobacteria, the light energy is transferred through antenna complexes to the reaction center (RC) of the photosystem II (PSII) in the thylakoid membrane. The RC is composed of the D1/D2 heterodimer, possessing the chlorophyll a (Chla) pair (P_{D1}/P_{D2}), the accessory Chla (Chl_{D1}/Chl_{D2}), the pheophytins ($Pheo_{D1}/Pheo_{D2}$), two quinones, and two additional Chla as the redox active cofactors.[1] It has been suggested that the electron is transferred to $Pheo_{D1}$ from $^1Chl_{D1}$* electronically excited via the antenna, following hole-transfer to the "special pair (P)" of P_{D1}/P_{D2} generating the primary charge-separated (CS) state of $P^{+\bullet}$ $Pheo_{D1}^{-\bullet}$.[2-4] Subsequently, the electron is transferred from $Pheo_{D1}^{-\bullet}$ to the secondary acceptor quinone (Q_A).[2] On the donor site, the hole is transferred from $P^{+\bullet}$ to a tyrosine residue (Tyr_Z) nearby P_{D1}.[2, 5] The oxidation states in the Mn_4CaO_5 cluster are then generated resulting in the splitting of water to produce the molecular oxygen by utilizing their chemical potentials.[6] If Q_A is pre-reduced or depleted, the electron-transfer (ET) reaction is blocked at $Pheo_{D1}$ and therefore, the primary CS state is deactivated by the triplet recombination.[7] Lubitz and co-workers suggested that the excited triplet state generated by the charge-recombination (CR) resides in Chl_{D1} from a time-resolved electron paramagnetic resonance (TREPR) measurements at a cryogenic temperature.[8] Several studies have been performed to understand mechanisms of an extremely high redox potential of $P^{+\bullet}$ in PSII while the photosynthetic reaction centers (PRC) do not have such potentials in purple bacteria.[9-12] For chemically oxidized PSII RC samples, the cationic charge was reported to be localized on the D1 part (P_{D1}) at 70-80 % over P_{D1}/P_{D2},[9-10] lowering the singly occupied molecular orbital (SOMO) level to oxidize the Mn_4CaO_5 cluster. On the primary CS state, Matysik et al.[12] demonstrated that the cationic charge is localized at a single Chla site by using the photo-CIDNP method. Ultrafast spectroscopic studies have also denoted the predominance of the cationic charges on

the D1 part in the primary CS states (namely, $P_{D1}^{+\bullet}$ $Pheo_{D1}^{-\bullet}$) as the short-lived intermediate in the PSII reaction centers.[3]

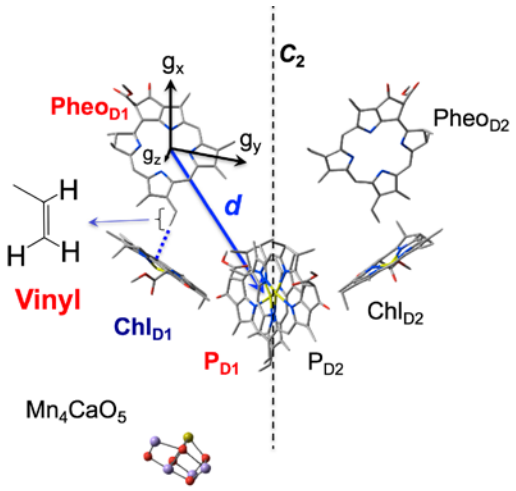

Figure 1. X-ray structure of the cofactors in PSII reaction center taken from a PDB code 3ARC. Reference protein axes are set in (g_x, g_y, g_z) in $Pheo_{D1}$ to express the direction (***d***) of the spin dipolar coupling and the pseudo C_2 symmetry axis (***C***$_2$).

In the primary CS states, the above oxidative and localized cationic charge would cause a strong electronic interaction with $Pheo_{D1}^{-\bullet}$ and thus suffer from an energy-wasting CR process, since the distance between the charges is expected to be shorter in PSII than in the purple bacteria[12] in which the hole distribution is highly delocalized on the special pair. However, no experimental studies have been performed to understand how cofactor geometries play roles on the electronic interaction of the primary CS state in which the anionic charge may significantly influence the electronic state. In particular, $Pheo_{D1}$ employs a vinyl group as a terminal substituent which is located in close proximity to Chl_{D1} as shown in Figure 1, whereas the bacterial pheophytin (H_A) utilizes an acetyl group as one of the electron-tunneling routes between the accessory chlorophyll (B_A) and H_A.[13] It has been unclear how the vinyl substituent plays a role on the electronic couplings for the initial light-energy conversion in the plants. We

have herein observed the primary CS states in quinone pre-reduced membranes of PSII from spinach in frozen solution and in oriented multilayers at 77 K using the X-band TREPR method. We show that, although the cationic charge is localized at P_{D1} and the molecular conformation of $Pheo_{D1}$ is conserved after the primary charge-separations, the electronic coupling between the charges is significantly weak.

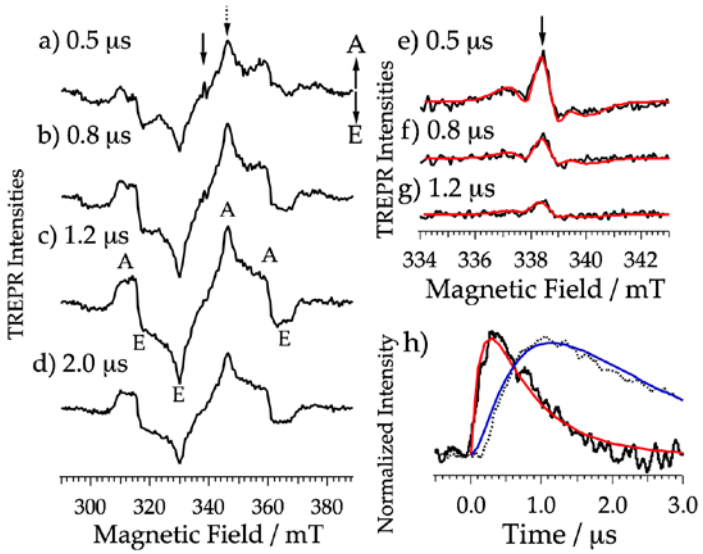

Figure 2. a–d) TREPR spectra of the quinone doubly-reduced membrane of PSII in buffer/glycerol solution at several delay times at T = 77 K. e–g) Zoom-in views of the TREPR spectra at the center field regions of 338 mT obtained after baseline corrections, showing the primary CS state. h) Time profiles of the peaks at 338.3 mT (solid line) and at 345 mT (dotted line). The colored lines in e)-h) are computed TREPR signals obtained by the powder-pattern calculations of the transverse magnetizations.

Figure 2a–d show TREPR spectra of the quinone doubly-reduced membrane of PSII from spinach in frozen solution at 77 K obtained by the 532 nm pulsed laser irradiations. At the later delay time of 1.2 µs in Figure 2c, a broad A/E/E/A/A/E polarization pattern, where A and E denote microwave absorption and emission, respectively, is assigned to the fine structure of the recombined $^3Chl_{D1}$* after singlet-triplet (S–T_0) conversion of the primary CS state.[8] A minor

broad signal by the triplet carotenoid[14] is superimposed in Figure 2a-d as detailed in Figure S1 of Supporting Information. In the early delay times before 1 μs, one can see sharp signals as indicated by a solid arrow in Figure 2a. To obtain the sharp spectrum components at the center region (Figure 2e–g), each TREPR spectrum in Figure 2a-c has been subtracted from the sigmoid line–shape at the delay time of 2.0 μs (Figure 2d) for the magnetic field ($\boldsymbol{B}_0$) from 334 to 343 mT, as shown in Figure S2 of Supporting Information. The expanded spectrum of the sharp component in Figure 2e exhibits an A/A/E/E fine structure with a distorted shape and is changed to the weak absorptive signal in Figure 2g by increasing the delay time. Figure 2h shows time profiles of the EPR signals of the sharp component at 338.3 mT (solid line) and of the absorptive peak at 345.0 mT (indicated by the dotted arrow in Figure 2a) due to the recombined $^3Chl_{D1}$*. The decay lifetime (0.5 μs) of the solid line is coincident with the rise time of the dotted line. It is known, in the PSII RC, that the primary CS state of $P^{+\bullet}Pheo_{D1}^{-\bullet}$ is deactivated by transferring both the electron and the hole to Chl_{D1} to generate $^3Chl_{D1}$* as the CR product.[15] Thus, the A/A/E/E pattern in Figure 2e is attributable to the primary CS state of $P^{+\bullet}Pheo_{D1}^{-\bullet}$.

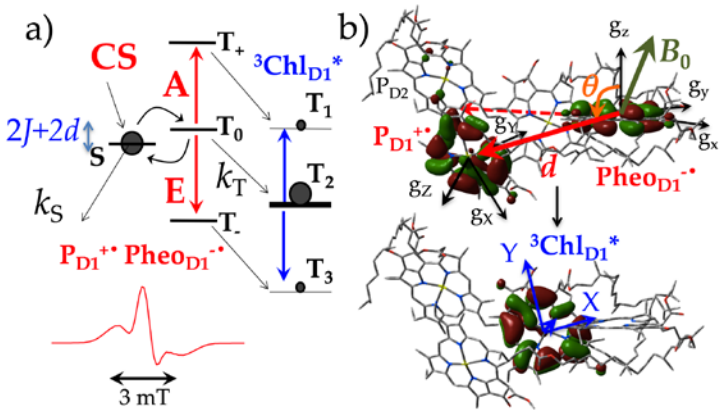

Figure 3. a) Quantum mechanical electron spin polarization model to compute the TREPR spectrum (bottom) by the primary singlet CS and the subsequent triplet CR leading to the T_1, T_2 and T_3 spin states in the presence of $\boldsymbol{B}_0$. b) Geometries of the primary CS state (top) and of the recombined $^3Chl_{D1}$* (bottom) taken from the X-ray structure.

By the spin correlated radical pair (SCRP) model,[16-18] the EPR spectrum shape is highly affected by the electron spin–spin dipolar coupling (***d***), the spin–spin exchange coupling (J) and the spin multiplicity of the precursor excited state to generate the CS states. We have calculated time developments of the transient EPR intensities by numerical analysis of the coupled stochastic–Liouville equation (SLE)[19] on the basis spin functions of S, T_+, T_0, T_- in $P^{+\bullet}Pheo_{D1}^{-\bullet}$ and T_1, T_2, T_3 spin states in $^3Chl_{D1}$*, as shown in Figure 3a. With applying principal axis orientations in $P^{+\bullet}$ and $Pheo_{D1}^{-\bullet}$,[20-21] as described in the Supporting Information, the g–tensors ($\boldsymbol{G}_P$ and $\boldsymbol{G}_{Pheo}$) have been computed in a reference axis system of X'–Y'–Z' represented by the principal axes of the ***d*** coupling. We have taken into account J, ***d***, isotropic and anisotropic hyperfine couplings (HFC), and relaxation kinetics by the singlet and triplet CRs (k_S and k_T in Figure 3a)[19] and by the spin–relaxations, as detailed in Supporting Information with Figure S3. In the present X-band EPR calculation, the computed spectrum was not significantly affected by the orientations of $\boldsymbol{G}_P$. This is because the g-anisotropy is small (g_{Px} = 2.00329, g_{Py} = 2.00275, and g_{Pz} = 2.00220)[20] in $P^{+\bullet}$. Thanks to large magnetic anisotropies in ***d*** and in HFC of $Pheo_{D1}^{-\bullet}$, however, the EPR spectrum shape obtained by the powder-pattern integration from all the possible field directions was highly dependent on the ***d***-direction (θ and ϕ defined as the polar and azimuthal angles with respect the principal axes of the g-tensor in $Pheo^{-\bullet}$) in Figure 3b or on the conformation of the $Pheo_{D1}^{-\bullet}$. (See Figure S4.) Concerning the anisotropic magnetic interactions, the following parameters have been utilized based upon the X-ray structure: 1) the spin-dipolar coupling (as characterized by D_{RP} = –0.75 mT and E_{RP} = 0.04 mT) which is dependent of the $\boldsymbol{B}_0$-direction of $\boldsymbol{e}$ = (l, m, n), as expressed by $d = D_{RP}(n^2–1/3)/2 + E_{RP}(l^2–m^2)$ with the inter–spin vector ***d*** (= Z' axis) directing to (θ, ϕ) = (99°, –140°) in the (g_x, g_y, g_z) axis system from $Pheo_{D1}^{-\bullet}$ to $P_{D1}^{+\bullet}$ (red solid arrow in Figure 3b), and 2) the nitrogen hyperfine

tensors of (A_{xx}, A_{yy}, A_{zz}) = (0.0, 0.0, 0.82) mT in $Pheo_{D1}^{-\bullet}$.[13] Both the TREPR spectra and their time evolutions have been reproduced as shown by the red lines in Figure 2e–h by using J = –0.20 mT, k_S = 0.5 μs^{-1}, k_T = 1.5 μs^{-1} and T_{1RP} = 0.5 μs as the spin–lattice relaxation time. k_T = 1.5 μs^{-1} is in line with a reported submicrosecond recombination kinetics of the CS state obtained by the transient absorption method on the quinone pre-reduced PSII membrane.[22] The quick spin relaxation for T = 77 K may originate from librational charge motions to induce fluctuations of the J-coupling[23] in the primary CS state due to low-frequency cofactor motions to cause the cationic charge redistributions in the special pairs, as predicted by the molecular dynamics simulation.[11] The time–development of the triplet EPR signal at 345 mT has also been reproduced as shown by the blue line in Figure 2h, by applying the triplet–triplet electron spin polarization transfer model in Figure 3a[24] using the principal axes (X,Y,Z) of the tensor orientation (α, β, γ) = (55°, 74°, 15°) on the zero field splitting (ZFS) interaction of $^3Chl_{D1}$* obtained from the single–crystal TREPR study.[8] From D_{RP} = –0.75 mT, the CS distance is estimated to be r_{CC} = 1.5 nm by the point–dipole approximation of $D_{RP} \approx -(3/2)(g\beta)^2/r_{CC}^3$. This is consistent with the center–to–center distance between $Pheo_{D1}$ and P_{D1} from the X-ray structure in Figure 3b.

To confirm the above assignment of the center field spectra (Figure 2e-g) as the primary CS state and to obtain validities both of the molecular geometries and J, we have observed the TREPR spectra for the oriented multilayer[21] of PSII on a plastic sheet, as shown in Figure 4. Figure 4a and 4b show entire views of the TREPR spectra at the sample orientation that normal vectors from the sheet plane are parallel (θ_{MB} = 0) and perpendicular (θ_{MB} = π/2) to the $\boldsymbol{B}_0$ directions, respectively, at a delay time of 0.8 μs. It is known that the membrane normal vector $\boldsymbol{C}_2$ coincides with the pseudo C_2 symmetric axis in Figure 1 and is preferentially oriented

perpendicular to the plastic sheet.[21] Thus, Figure 4a and 4b are attributable to $\boldsymbol{B}_0$ parallel and perpendicular to $\boldsymbol{C}_2$, respectively.

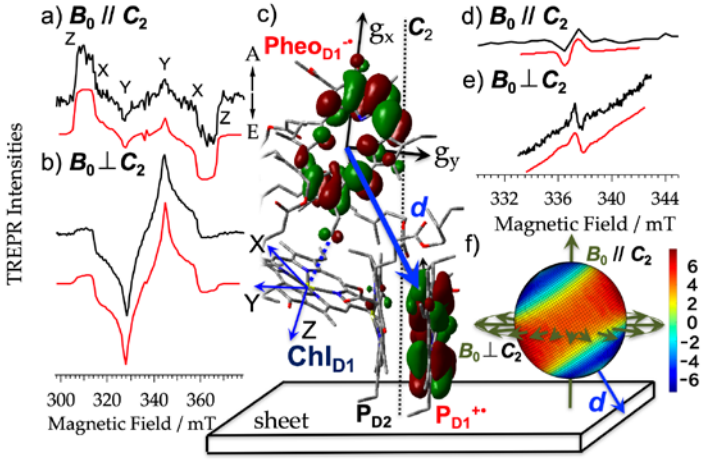

Figure 4. TREPR data of the quinone pre–reduced PSII membranes oriented as the multilayers on a plastic sheet. a) and b) were obtained for the sample orientations that the $\boldsymbol{C}_2$ axis is parallel and perpendicular to $\boldsymbol{B}_0$, respectively, at a delay time of 0.8 μs. c) Cofactor orientations are shown with respect to the $\boldsymbol{C}_2$ axis as taken from the X-ray structure. d–e) The TREPR spectra at the center field regions of 337 mT for the d) parallel and e) perpendicular orientations at 0.5 μs. Computed spectra are shown by the red lines in a), b), d) and e) for the corresponding sample orientations and the delay times. f) 3D spin polarization imaging mapped to all possible $\boldsymbol{B}_0$ directions at 338.3 mT as computed from the powder-pattern TREPR spectrum of Figure 2e. The red area denote that the A/E polarization is strong, while the blue region corresponds to the strong E/A polarization.

Since the spatial orientations of the ZFS principal axes of X-Y-Z and $\boldsymbol{d}$ (Figure 4c) are both modulated by the sample rotations (θ_{MB}) with respect to the laboratory frame, one can characterize the conformations of X-Y-Z and $\boldsymbol{d}$ by introducing a distribution function[25] in the $\boldsymbol{B}_0$-direction angle, as detailed in Supporting Information. In fact, an enhanced A/E-polarized Z-transitions is observed in Figure 4a, while an enhanced E/A Y-transition is detected in Figure 4b. These are both coincident with the residence of the triplet product at Chl_{D1} by the geminate CR, since the principal Z and Y axes are roughly parallel and perpendicular to the $\boldsymbol{C}_2$ axis,

respectively in Figure 4c. Figure 4d and 4e show the TREPR spectra at the center field regions at the earlier delay time of 0.5 μs for θ_{MB} = 0 and π/2, respectively, corresponding to the primary CS states in Figure 2e. The spectrum pattern (E/A or A/E) is clearly dependent on the sample orientation in Figure 4d and 4e. To obtain a clearer 3D view how the spin polarization of the SCRP is modulated by the $\boldsymbol{B}_0$-direction, we mapped in Figure 4f a $\boldsymbol{B}_0$-direction dependence of the absorptive or emissive EPR intensity at a lower field strength (338.3 mT in Figure 2e) obtained from the computed powder-pattern TREPR spectrum that reproduced Figure 2e. From the color legend in Figure 4f, the red color represents the strong microwave absorption, while the blue one corresponds to the strong emission at 338.3 mT. The blue emissive regions thus represent that the E/A polarization is generated when the $\boldsymbol{B}_0$-direction is close to the inter–spin Z' axis (***d***-vectors in Figure 4), while the red area specifies that the A/E polarization is generated when $\boldsymbol{B}_0$ is directing perpendicular to the ***d*** based upon the transition scheme in Figure 3a. This is because the sign of *d* depends on the $\boldsymbol{B}_0$-direction, as expressed above. This color map thus explains that the powder-pattern spectrum shape in Figure 2e is strongly contributed by ***d***. From Figure 4c and 4f, it is predicted that the E/A polarization is detected when $\boldsymbol{B}_0$ is parallel to $\boldsymbol{C}_2$, while the A/E polarization is obtained for the $\boldsymbol{B}_0$ perpendicular to $\boldsymbol{C}_2$, as shown by the green $\boldsymbol{B}_0$-vectors on the imaging view of Figure 4f. The experimental results in Figure 4d and 4e are well coincident with this prediction, strongly supporting the assignments of the TREPR spectra as $P_{D1}^{+\bullet}Pheo_{D1}^{-\bullet}$. This also implies that the ***d*** coupling is stronger than the isotropic coupling of J = –0.2 mT. We conducted the model calculations (red lines in Figure 4) of the EPR transitions (Figure 3a) with setting a distribution angle[21] of Δ = 20° on the CS state, as detailed in Supporting Information. Experimental spectra in Figure 4d and 4e were well reproduced using J = –0.2 mT, D_{RP} = –0.75 mT and E_{RP} = 0.04 mT with (θ, ϕ) = (99°, –140°). We also performed

the calculations in Figure S5 on the θ_{MB} effects of the TREPR spectra of the CS state for another set of the input parameters: D_{RP} = –0.50 mT and E_{RP} = 0.08 mT with (θ, ϕ) = (90°, –140°) representing that the hole is fully delocalized in P_{D1}/P_{D2}, as in the special pair of the PRC, which is identified by the dotted ***d*** vector with r_{CC} = 1.8 nm in Figure 3b.[16, 19] This parameter set produced highly deviated spectra from the experiments, excluding the delocalized hole distribution in the CS state as shown in Figure S5. The agreements of the red lines in Figure 2 and 4 with the experimental spectra thus demonstrate that the cofactor conformation in $Pheo_{D1}^{-\bullet}$ are unchanged by the ET and that the hole is localized at $P_{D1}^{+\bullet}$, as shown in Figure 4b, indicating that the electron tunneling route in $Chl_{D1}\cdots Pheo_{D1}$ is not disrupted, as shown by the dotted line in Figure 4c. From the localized electron and hole at r_{CC} = 1.5 nm, a strong electrostatic stabilization is anticipated. This may avoid the Tyr_Z oxidization to produce the CS state of $Tyr_Z^{\bullet}(H^+)\cdots Pheo_{D1}^{-\bullet}$ from $P_{D1}^{+\bullet}\cdots Pheo_{D1}^{-\bullet}$. When Q_A is not pre-reduced, however, the subsequent ET from $Pheo_{D1}^{-\bullet}$ to Q_A will eliminate this electrostatic stabilization, resulting in $Tyr_Z^{\bullet}(H^+)\cdots Q_A^{-\bullet}$ via $P^{+\bullet}\cdots Q_A^{-\bullet}$.[5] The above electrostatic interaction by $Pheo_{D1}^{-\bullet}$ might cause the more localized cationic charge distribution[12] than the distribution[8] at 70-80 % on P_{D1} in the chemically oxidized PSII sample, contributing to the strong ***d***-coupling.

The *J*-coupling is revealed to be much weaker (–0.2 mT) in the present CS state than *J* = –0.9 mT in $P^{+\bullet}H_A^{-\bullet}$ despite the shorter inter-spin distance of 1.5 nm in PSII than in the purple bacteria.[16, 19] In the PSII RC, $P_{D1}^{+\bullet}Pheo_{D1}^{-\bullet}$ is deactivated by transferring both the electron and the hole to Chl_{D1} producing $^3Chl_{D1}$* as the CR product.[15] This one-step recombination is viewed as the superexchange ET mediated by a virtual state of $P_{D1}^{+\bullet}\cdots Chl_{D1}^{-\bullet}\cdots Pheo_{D1}$ which energy is higher by ΔE than $P_{D1}^{+\bullet}\cdots Chl_{D1}\cdots Pheo_{D1}^{-\bullet}$. The ET sequence described by $P_{D1}^{+\bullet}\cdots Chl_{D1}\cdots Pheo_{D1}^{-\bullet}$ –> $P_{D1}^{+\bullet}\cdots Chl_{D1}^{-\bullet}\cdots Pheo_{D1}$ –> $P_{D1}\cdots Chl_{D1}^*\cdots Pheo_{D1}$ is then useful to evaluate the bridge-

mediated electronic coupling (V_{CR}) for this one-step recombination,[26] that is $|V_{CR}| = |V_{Pheo}||V_{PD1}|/\Delta E$, where $|V_{Pheo}|$ is the transfer-integral between the lowest unoccupied molecular orbitals (LUMO) of Chl_{D1} and $Pheo_{D1}$. Similarly, $|V_{PD1}|$ denotes the transfer-integral between the highest occupied molecular orbitals (HOMO) of P_{D1} and Chl_{D1}. ΔE = 2,040 cm^{-1} was estimated as the vertical tunneling energy gap.[19, 27] By this V_{CR} interaction, the *J*-coupling is induced as the configuration interaction from the excited states of Chl_{D1}*.[28] In the purple bacteria, $|V_{CR}| = |V_{BH}||V_{PB}|/\Delta E$ has been considered from the superexchange mechanism.[19, 26] Here, $|V_{BH}|$ is the transfer-integral between H_A and the bacteria chlorophyll (B_A) and corresponds to $|V_{Pheo}|$ in the present study. $|V_{CR}|$ = 2.2 cm^{-1} was obtained from J = –0.9 mT in $P^{+\bullet}$ $H_A^{-\bullet}$.[19] Since J is proportional to $|V_{CR}|^2$,[19, 26] $|V_{CR}|$ = 1.0 cm^{-1} is evaluated from J = –0.2 mT in $P_{D1}^{+\bullet}$ $Pheo_{D1}^{-\bullet}$. The CR rate of k_T = 1.5 μs^{-1} is smaller in the PSII than k_T = 400 μs^{-1} in the bacterial PRC.[16, 19, 29] These triplet recombination processes are both activationless,[22, 27] as described in Supporting Information. Thus, the present weaker *J*-coupling (–0.2 mT) is consistent with the smaller k_T, since k_T is proportional to $|V_{CR}|^2$.[30] This means that the electronic coupling between the unpaired orbitals is weaker even for the closer separation distance of 1.5 nm in $P_{D1}^{+\bullet}$ $Pheo_{D1}^{-\bullet}$ than in $P^{+\bullet}$ $H_A^{-\bullet}$ of the purple bacteria.

In PSII, the vinyl group of $–CH=CH_2$ is directing to Chl_{D1} as shown in Figure 1 and 4c, whereas the acetyl group $–C(CH_3)=O$ is substituted in H_A as the electron-tunneling route[11] generating $|V_{BH}|$ = 135 cm^{-1} for $B_A^{-\bullet}\cdots H_A$ –> $B_A\cdots H_A^{-\bullet}$ in the purple bateria.[13] The vinyl group in the plant may restrict the $|V_{Pheo}|$ coupling and thus weaken the electronic interaction in the CS state. When $|V_{Pheo}| = |V_{PD1}|$ is assumed, $|V_{Pheo}|$ = 45 cm^{-1} is estimated for the dotted interaction in Figure 4c from $|V_{CR}| = |V_{Pheo}||V_{PD1}|/\Delta E$ and $|V_{CR}|$ = 1.0 cm^{-1}. This significantly weaker coupling is rationalized by the lower electron affinity (EA = -1.55 eV) of ethylene[31] than EA = 0.0 eV in

acetaldehyde,[32] since such a low EA will restrict the hybridization of LUMO in the vinyl group with the electron-accepting frontier orbital in the aromatic ring plane. This is in line with the smaller spin density at the vinyl group in $Pheo^{-\bullet}$ than the spin density at the acetyl group in $H_A^{-\bullet}$, as reported by O'Malley.[13] Moreover, $|V_{Pheo}| < |V_{BH}|$ is well consistent with the slower time scale (37 ps)[4] in the forward ET from $Chl_{D1}^{-\bullet}$ to $Pheo_{D1}$ than $\approx$ 1 ps in the ET[33] from $B_A^{-\bullet}$ to H_A of the purple bacteria.

In conclusion, we have characterized the geometry, the orientation, and the electronic character of the primary CS state in the PSII using the TREPR method. The localized hole distribution at $P_{D1}^{+\bullet}$ which is essential in oxidizing Mn_4CaO_5 has been demonstrated in the primary CS state with r_{CC} = 1.5 nm. The weak *J*-coupling between $P_{D1}^{+\bullet}$ and $Pheo_{D1}^{-\bullet}$ is explained by the limited spin density at the terminal vinyl group in $Pheo_{D1}^{-\bullet}$, regulating the orbital overlap between Chl_{D1} and $Pheo_{D1}^{-\bullet}$ to inhibit the energy-wasting recombination for the close separation distance between the cofactors in Figure 4c. Above fundamental characteristics of the regulated cofactor-cofactor interactions of the primary CS state are essential keys to the artificial light-energy conversion systems and are informative for understanding the evolutions of the molecular engineering in the higher plants.

ASSOCIATED CONTENT

Supporting Information. The Supporting Information is available free of charge on the ACS Publications website.

Sample preparations, experimental methods, and the computation methods. (file type, PDF)

AUTHOR INFORMATION

Notes

The authors declare no competing financial interests.

ACKNOWLEDGMENT

This work was supported by a Grant-in-Aid for Scientific Research (No. 25288004, 26620065 and 16H04097 to Y. Kobori) from the Ministry of Education, Culture, Sports, Science and Technology, Japan.

REFERENCES

(1) Umena, Y.; Kawakami, K.; Shen, J.-R.; Kamiya, N. Crystal structure of oxygen-evolving photosystem II at a resolution of 1.9 A. *Nature* **2011,** *473* 55-60.

(2) Cardona, T.; Sedoud, A.; Cox, N.; Rutherford, A. W. Charge separation in Photosystem II: A comparative and evolutionary overview. *Biochim. Biophys. Acta* **2012,** *1817* 26-43.

(3) Groot, M. L.; Pawlowicz, N. P.; van Wilderen, L. J. G. W.; Breton, J.; van Stokkum, I. H. M.; van Grondelle, R. Initial electron donor and acceptor in isolated Photosystem II reaction centers identified with femtosecond mid-IR spectroscopy. *Proc. Natl. Acad. Sci. U. S. A.* **2005,** *102* 13087-13092.

(4) Romero, E.; van Stokkum, I. H. M.; Novoderezhkin, V. I.; Dekker, J. P.; van Grondelle, R. Two Different Charge Separation Pathways in Photosystem II. *Biochemistry* **2010,** *49* 4300-4307.

(5) Zech, S. G.; Kurreck, J.; Eckert, H.-J.; Renger, G.; Lubitz, W.; Bittl, R. Pulsed EPR measurement of the distance between $P680^{+\cdot}$ and $QA^{-\cdot}$ in photosystem II. *FEBS Lett.* **1997,** *414* 454-456.

(6) Rappaport, F.; Diner, B. A. Primary photochemistry and energetics leading to the oxidation of the (Mn)4Ca cluster and to the evolution of molecular oxygen in Photosystem II. *Coord. Chem. Rev.* **2008,** *252* 259-272.

(7) van Mieghem, F.; Brettel, K.; Hillman, B.; Kamlowski, A.; Rutherford, A. W.; Schlodder, E. Charge Recombination Reactions in Photosystem II. 1. Yields, Recombination Pathways, and Kinetics of the Primary Pair. *Biochemistry* **1995,** *34* 4798-4813.

(8) Kammel, M.; Kern, J.; Lubitz, W.; Bittl, R. Photosystem II single crystals studied by transient EPR: the light-induced triplet state. *Biochim. Biophys. Acta* **2003,** *1605* 47-54.

(9) Okubo, T.; Tomo, T.; Sugiura, M.; Noguchi, T. Perturbation of the Structure of P680 and the Charge Distribution on Its Radical Cation in Isolated Reaction Center Complexes of Photosystem II as Revealed by Fourier Transform Infrared Spectroscopy. *Biochemistry* **2007,** *46* 4390-4397.

(10) Saito, K.; Ishida, T.; Sugiura, M.; Kawakami, K.; Umena, Y.; Kamiya, N.; Shen, J.-R.; Ishikita, H. Distribution of the Cationic State over the Chlorophyll Pair of the Photosystem II Reaction Center. *J. Am. Chem. Soc.* **2011,** *133* 14379-14388.

(11) Narzi, D.; Bovi, D.; De Gaetano, P.; Guidoni, L. Dynamics of the Special Pair of Chlorophylls of Photosystem II. *J. Am. Chem. Soc.* **2016,** *138* 257-264.

(12) Matysik, J.; Alia; Gast, P.; van Gorkom, H. J.; Hoff, A. J.; de Groot, H. J. M. Photochemically induced nuclear spin polarization in reaction centers of photosystem II observed by 13C-solid-state NMR reveals a strongly asymmetric electronic structure of the $P680^{\cdot+}$ primary donor chlorophyll. *Proc. Natl. Acad. Sci. U. S. A.* **2000,** *97* 9865-9870.

(13) O'Malley, P. J. Hybrid Density Functional Studies of Pheophytin Anion Radicals: Implications for Initial Electron Transfer in Photosynthetic Reaction Centers. *J. Phys. Chem. B* **2000,** *104* 2176-2182.

(14) Di Valentin, M.; Biasibetti, F.; Ceola, S.; Carbonera, D. Identification of the Sites of Chlorophyll Triplet Quenching in Relation to the Structure of LHC-II from Higher Plants. Evidence from EPR Spectroscopy. *J. Phys. Chem. B* **2009,** *113* 13071-13078.

(15) Noguchi, T.; Tomo, T.; Kato, C. Triplet formation on a monomeric chlorophyll in the photosystem II reaction center as studied by time-resolved infrared spectroscopy. *Biochemistry* **2001,** *40* 2176-2185.

(16) Till, U.; Klenina, I. B.; Proskuryakov, I. I.; Hoff, A. J.; Hore, P. J. Recombination dynamics and EPR spectra of the primary radical pair in bacterila photosynthetic reaction centers with blocked electron transfer to the primary acceptor. *J. Phys. Chem. B* **1997,** *101* 10939-10948.

(17) Weber, S.; Biskup, T.; Okafuji, A.; Marino, A. R.; Berthold, T.; Link, G.; Hitomi, K.; Getzoff, E. D.; Schleicher, E.; Norris, J. R. Origin of Light-Induced Spin-Correlated Radical Pairs in Cryptochrome. *J. Phys. Chem. B* **2010,** *114* 14745-14754.

(18) Closs, G. L.; Forbes, M. D. E.; Norris, J. R. Spin-Polarized Electron-Paramagnetic Resonance-Spectra of Radical Pairs in Micelles - Observation of Electron-Spin Spin Interactions. *J. Phys. Chem.* **1987,** *91* 3592-3599.

(19) Kobori, Y.; Ponomarenko, N.; Norris, J. R. Time-Resolved Electron Paramagnetic Resonance Study on Cofactor Geometries and Electronic Couplings after Primary Charge Separations in the Photosynthetic Reaction Center. *J. Phys. Chem. C* **2015,** *119* 8078-8088.

(20) Bratt, P. J.; Poluektov, O. G.; Thurnauer, M. C.; Krzystek, J.; Brunel, L.-C.; Schrier, J.; Hsiao, Y.-W.; Zerner, M.; Angerhofer, A. The g-Factor Anisotropy of Plant Chlorophyll $a^{\bullet+}$. *J. Phys. Chem. B* **2000,** *104* 6973-6977.

(21) Dorlet, P.; Rutherford, A. W.; Un, S. Orientation of the Tyrosyl D, Pheophytin Anion, and Semiquinone $Q^{A\bullet-}$ Radicals in Photosystem II Determined by High-Field Electron Paramagnetic Resonance. *Biochemistry* **2000,** *39* 7826-7834.

(22) Hillmann, B.; Brettel, K.; van Mieghem, F.; Kamlowski, A.; Rutherford, A. W.; Schlodder, E. Charge Recombination Reactions in Photosystem II. 2. Transient Absorbance Difference Spectra and Their Temperature Dependence. *Biochemistry* **1995,** *34* 4814-4827.

(23) Fukuju, T.; Yashiro, H.; Maeda, K.; Murai, H.; Azumi, T. Singlet-born SCRP observed in the photolysis of tetraphenylhydrazine in an SDS micelle: Time dependence of the population of the spin states. *J. Phys. Chem. A* **1997,** *101* 7783-7786.

(24) Kobori, Y.; Fuki, M.; Murai, H. Electron Spin Polarization Transfer to the Charge-Separated State from Locally Excited Triplet Configuration. Theory and Its Application to Characterization of Geometry and Electronic Coupling in the Electron Donor-Acceptor System. *J. Phys. Chem. B* **2010,** *114* 14621-14630.

(25) Nagashima, H.; Mino, H. Highly resolved proton matrix ENDOR of oriented photosystem II membranes in the S2 state. *Biochim. Biophys. Acta* **2013,** *1827* 1165-1173.

(26) Bixon, M.; Jortner, J.; Michelbeyerle, M. E.; Ogrodnik, A. A Superexchange Mechanism for the Primary Charge Separation in Photosynthetic Reaction Centers. *Biochim. Biophys. Acta* **1989,** *977* 273-286.

(27) Volk, M.; Aumeier, G.; Langenbacher, T.; Feick, R.; Ogrodnik, A.; Michel-Beyerle, M. E. Energetics and mechanism of primary charge separation in bacterial photosynthesis. A comparative study on reaction centers of *Rhodobacter sphaeroides* and *Chloroflexus aurantiacus*. *J. Phys. Chem. B* **1998,** *102* 735-751.

(28) Anderson, P. W. New Approach to the Theory of Superexchange Interactions. *Phys. Rev.* **1959,** *115* 2-13.

(29) Michel-Beyerle, M. E.; Bixon, M.; Jortner, J. Interrelationship between primary electron transfer dynamics and magnetic interactions in photosynthetic reaction centers. *Chem. Phys. Lett.* **1988,** *151* 188-194.

(30) Marcus, R. A.; Sutin, N. Electron transfer in chemistry and biology. *Biochim. Biophys. Acta* **1985,** *811* 265-322.

(31) Burrow, P. D.; Jordan, K. D. On the electron affinities of ethylene and 1,3-butadiene. *Chem. Phys. Lett.* **1975,** *36* 594-598.

(32) Desfrançois, C.; Abdoul-Carime, H.; Khelifa, N.; Schermann, J. P. From 1/r to $1/r^2$ Potentials: Electron Exchange between Rydberg Atoms and Polar Molecules. *Phys. Rev. Lett.* **1994,** *73* 2436-2439.

(33) Zinth, W.; Wachtveitl, J. The first picoseconds in bacterial photosynthesis - Ultrafast electron transfer for the efficient conversion of light energy. *ChemPhysChem* **2005,** *6* 871-880.